Semiempirical van der Waals method for two-dimensional materials with incorporated dielectric functions

Xiaofei Liu,* Jiabao Yang, and Wanlin Guo†

State Key Laboratory of Mechanics and Control of Mechanical Structures, Key Laboratory for Intelligent Nano Materials and Devices of the Ministry of Education, Nanjing University of Aeronautics and Astronautics, 210016 Nanjing, China

(Received 30 May 2019; revised manuscript received 15 December 2019; published 23 January 2020)

A density functional theory based semiempirical van der Waals (vdW) method with dielectric functions being incorporated is developed for two-dimensional materials. The coefficients of interatomic pairwise potentials are derived from atomic polarizabilities obtained via a Clausius-Mossotti relation dedicated for layered crystals. The method not only can efficiently describe the dispersion energy for a range of planar graphene-like materials at nearly the same accuracy as the adiabatic connection fluctuation-dissipation theorem, but also rationalizes experimentally measured relative interfacial strengths of heterostructures and interlayer registry of hexagonal boron nitride that have plagued other vdW methods.

DOI: 10.1103/PhysRevB.101.045428

I. INTRODUCTION

The van der Waals (vdW) interaction is an essential form of intermolecular interaction that complements other strong interactions in assembling atoms into condensed matter [1]. The vdW interaction in two-dimensional (2D) materials has received the most attention because 2D materials not only are held together by such a weak interaction but also allow direct access of this interaction to all atoms constituting the crystals [2,3]. As a result, the vdW interaction can cause significant structural reconstruction at interfaces of 2D materials and gives rise to a series of fascinating properties via interfacial adjustments, including interlayer superlubricity [4] and soliton motion [5] as well as carrier localization [6] and even superconductivity in bilayered graphene at "magic" twist angles [7]. Moreover, the vdW interaction also plays a crucial role in nucleation and growth of 2D materials on substrates and subsequent transfer for applications [8,9].

The vdW interaction in 2D materials can be described via two routes: *ab initio* methods based on quantum mechanical theory and (semi)empirical methods based on a summation of interatomic pairwise potentials. The former, such as random phase approximation (RPA) and second-order Møller-Plesset perturbation theory (MP2) [10–12], is accurate but the computationally affordable systems are limited in scale. While being highly desirable in practical 2D materials study because of low computational cost, the latter, such as the Grimme06 and Tkatchenko-Scheffler (TS) methods [13–17], is insufficient for some fundamental issues regarding interlayer interactions. First, it is difficult for the (semi)empirical methods to offer a vdW energy ranking of homogeneous 2D materials consistent with *ab initio* methods [18,19]. This deficiency can impede the understanding of role of vdW interaction in surface energy-related behaviors of different 2D materials, including wetting of water [20,21] and liquid exfoliation of 2D flake [22,23]. Second, relative interfacial strengths at different 2D heterostructures predicted by the (semi)empirical methods can be in conflict with experimental measurements [24]. Third, the experimental interlayer registry of hexagonal boron nitride (*h*-BN) cannot be reproduced faithfully by the (semi)empirical methods [16,25,26]. Last, the strain dependence of interlayer vdW energy has not been described (semi)empirically.

Materials dielectric response is a key ingredient for the vdW interaction. On the one hand, the dispersion energy comes from fluctuating electromagnetic field in dielectric media, as found by Lifshitz in his seminal work [27]. On the other hand, the RPA theory obtains accurate correlation energy from electronic density response functions or equivalently dielectric matrices [28]. Although the (semi)empirical methods actually rely on dielectric responses, C_6 coefficients are usually derived from the property of free atoms or dilute bodies instead of 2D materials. Here, we propose a density functional theory (DFT) based semiempirical vdW methods with dielectric functions being incorporated using a Clausius-Mossotti relation dedicated for 2D materials. The method thus reflects the important effect of electronic structures and bonding formation on the vdW interaction and reasonably addresses above-mentioned issues.

II. THEORETICAL DETAILS

We start the discussion from the Clausius-Mossotti relation that relates materials dielectric functions to atomic polarizabilities. Owing to the reduced dimensionality, 2D materials show dielectric responses distinctly different from bulk materials [29,30] and hence a new Clausius-Mossotti relation is required, as recently proposed by Dell'Anna and Merano for planar graphene-like monolayers [31]. In the in-plane direction, the relation between the surface polarization density $\vec{P}$ and electric field $\vec{E}$ reads $\vec{P} = \varepsilon_0 \chi \vec{E}$, where χ is the

*liuxiaofei@nuaa.edu.cn
†wlguo@nuaa.edu.cn

so-called surface susceptibility. From the microscopic view, $\vec{P} = \sum_i N_i \vec{p}_i$, where N_i is the surface density of atom and $\vec{p}_i = \alpha_i \varepsilon_0 \vec{E}^i_{loc}$, with α_i and $\vec{E}^i_{loc}$ being the atomic polarizability and local field at sublattice i, respectively. Then, the question is how to connect $\vec{E}^i_{loc}$ with $\vec{E}$. By considering the dipole-dipole coupling, the local fields at A and B sublattices were deduced as

$$\vec{E}^{(A)}_{loc} = \vec{E} + \frac{\alpha_A C_1}{4\pi a^3}\vec{E}^{(A)}_{loc} + \frac{\alpha_B C_2}{4\pi a^3}\vec{E}^{(B)}_{loc}, \quad (1)$$

$$\vec{E}^{(B)}_{loc} = \vec{E} + \frac{\alpha_B C_1}{4\pi a^3}\vec{E}^{(B)}_{loc} + \frac{\alpha_A C_2}{4\pi a^3}\vec{E}^{(A)}_{loc}, \quad (2)$$

where a is the lattice constant. The second term in the right-hand side of Eq. (1) stands for the local field at the A sublattice induced by dipoles at the rest equivalent sublattices, while the third term represents the contribution by dipoles at all B sublattices. For planar graphene-like monolayers, the constants C_1 and C_2 were derived to be 5.517 and 11.575, respectively.

We extend the Clausius-Mossotti relation to 2D materials of other crystal structures. For a buckled honeycomb lattice (e.g., silicene [32]), C_1 remains the same, but C_2 varies with the ratio of buckling height to lattice constant (Fig. S1 [33]). For transition metal dichalcogenide (MX_2) of the 2H phase [3,34], the $\vec{E}^i_{loc}$ vs $\vec{E}$ relation is

$$\vec{E}^{(M)}_{loc} = \vec{E} + \frac{\alpha_M C_1}{4\pi a^3}\vec{E}^{(M)}_{loc} + \frac{2\alpha_X C_2}{4\pi a^3}\vec{E}^{(X)}_{loc}, \quad (3)$$

$$\vec{E}^{(X)}_{loc} = \vec{E} + \frac{\alpha_X C_1}{4\pi a^3}\vec{E}^{(X)}_{loc} + \frac{\alpha_M C_2}{4\pi a^3}\vec{E}^{(M)}_{loc} + \frac{\alpha_X C_3}{4\pi a^3}\vec{E}^{(X)}_{loc}. \quad (4)$$

In Eq. (4), the fourth term denotes the local field at a given X site in the top layer induced by dipoles at all X sites in the bottom layer. Similar to the case of buckled honeycomb lattice, the constants C_2 and C_3 for MX_2 vary with the ratios of vertical M-X and X-X spacing to lattice constant, respectively, as shown in Supplementary Material Fig. S1 [33]. With above Clausius-Mossotti relations, the in-plane atomic polarizability for an elementary 2D material (e.g., graphene and silicene) can be calculated from the in-plane dielectric function that is obtainable from the RPA theory. However, in a binary material, a single χ does not suffice to solve α_i for two elements. To circumvent this problem, an approximation $\frac{\alpha_A}{\alpha_B} \approx \sqrt{C^{AA}_{6free}/C^{BB}_{6free}}$ is applied, where C^{AA}_{6free} and C^{BB}_{6free} are the vdW coefficients of free A and B atoms, respectively.

The remaining task is to describe the atomic polarizability in the out-of-plane direction, i.e., $\alpha^\perp$. For monoatomic layers (e.g., graphene, h-BN and silicene), $\alpha^\perp$ can be calculated from the polarizability volume per atom, since this sort of 2D materials have no macroscopic polarization in the out-of-plane direction [31]. The mean atomic polarizability in an isotropic 2D material can be written as $\alpha_i(i\omega) = \frac{2}{3}\alpha_i^{\parallel}(i\omega) + \frac{1}{3}\alpha_i^{\perp}(i\omega)$ [35]. Then, the frequency-dependent $\alpha_i(i\omega)$ is used to calculate the C_6 coefficient using the Casimir-Polder integral, i.e., $C_6^{ii} = \frac{3}{\pi}\int_0^\infty \alpha_i(i\omega)\alpha_i(i\omega)d\omega$ [36]. For 2D materials with thickness of more than one atom (e.g., MX_2), the same treatment of $\alpha^\perp$ will result in polarizabilities even higher than those of free atoms and therefore unreasonable C_6, due to additional polarization as a result of charge transfer between the top and bottom layers under a vertical electric field. As the Clausius-Mossotti relation for $\alpha^\perp$ is absent, we use the free-atom polarizability α_{free} to replace $\alpha^\perp$. Employing the London formula $C_{6ii} = \frac{3}{4}\eta_i(\alpha_i^0)^2$ with η_i and α_i^0 being the atomic effective frequency and static polarizability [37], we can assume $C_6 \approx (\frac{2}{3}\sqrt{C_{6\parallel}} + \frac{1}{3}\sqrt{C_{6free}})^2$, where $C_{6\parallel}$ is derived from the in-plane polarizability and C_{6free} is the free-atom coefficient from the work of Chu and Dalgarno [38].

Incorporating vdW potentials with the derived C_6 coefficients into DFT calculations enables a convenient evaluation of interlayer interactions for 2D materials. The vdW correction consists of a summation of interatomic pairwise potentials damped at small distances [13,14],

$$E_{vdW} = -\frac{1}{2}\sum_{A,B} f_{damp}(R^{AB}, R_0^A, R_0^B) C_6^{AB} (R^{AB})^{-6}, \quad (5)$$

where R^{AB} is the distance between atoms A and B, C_6^{AB} is the interatomic vdW coefficient, and R_0^A and R_0^B are the effective vdW radii. The C_6^{AB} coefficient can be calculated from the derived C_6 coefficients of atoms A and B [14],

$$C_6^{AB} = \frac{2C_6^{AA}C_6^{BB}}{\frac{\alpha_B}{\alpha_A}C_6^{AA} + \frac{\alpha_A}{\alpha_B}C_6^{BB}}, \quad (6)$$

where α_A and α_B is the static polarizability of atoms A and B, respectively. According to Eqs. (9) and (11) in Ref. [14], the effective vdW radius R_{0eff} can be calculated from the free-atom vdW radius R_{0free} and the derived C_6 as

$$R_{0eff} = \left(\frac{C_6}{C_{6free}}\right)^{\frac{1}{6}} R_{0free}. \quad (7)$$

The damping function f_{damp} takes a form of Fermi-type function as used in the TS method [14], with the parameters d and S_R for the Perdew-Burke-Ernzernhof (PBE) functional [39] being 20 and 0.94, respectively. We use a notation vdW^{2D} for the method here, whose results are compared to those with other theories, including Grimme's D2 [40], TS, many-body-dispersion (MBD) [41,42], and *ab initio* adiabatic-connection fluctuation-dissipation theorem (ACFDT-RPA).

The frequency dependent dielectric functions were obtained using the optical routine as implemented in the VASP code [43]. The standard projector-augmented wave method for the core region and the PBE functional for the exchange-correlation potential were employed. For the momentum sampling, the k-point meshes were set to be 35×35×1 and 25×25×1 for graphene (or h-BN) and other hexagonal 2D materials, respectively. To obtain optical spectra in the frequency range from 0 to 70 eV, bands no less than six times of default numbers were used. To study the interlayer interactions in a series of 2D structures, the PBE functional plus vdW correction strategies were applied. The DFT-TS, DFT-MBD and DFT-vdW^{2D} calculations were performed with the FHI-AIMS code [44] using the standard *tight* numeric atom-centered orbital basis, while those with the DFT-D2, ACFDT-RPA were carried out with the VASP code [43] using plane waves basis with an cutoff energy higher than 420 eV. To calculate the ACFDT-RPA correlation energies, k-point meshes of 11×11×1 and 10×10×1 were used for graphene (or h-BN) and other hexagonal 2D materials, respectively, with

TABLE I. C_6 coefficients (in unit of hartree bohr^6) and effective vdW radii (in units of bohr) of atoms in planar graphene-like monolayers derived from dielectric functions. The free-atom values as used in the TS method [14] are presented for comparison.

	GR	SiC	GeC	BN	BP	BAs	AlN	GaN	InN	SnC
a (Å)	2.46	3.10	3.28	2.46	3.21	3.39	3.13	3.25	3.59	3.60
$C_{6\text{free}}^{\text{AA}}$	44.6	305	354	99.5	99.5	99.5	528	496	707.0	587.4
$C_{6\text{free}}^{\text{BB}}$	–	44.6	44.6	24.2	185	246	24.2	24.2	24.2	44.6
$R_{0\text{free}}^{\text{A}}$	3.59	4.20	4.20	3.89	3.89	3.89	4.33	4.19	4.23	4.30
$R_{0\text{free}}^{\text{B}}$	–	3.59	3.59	3.34	4.01	4.11	3.34	3.34	3.34	3.59
$C_{6\text{vdW2D}}^{\text{AA}}$	17.63	125.82	166.65	27.41	52.29	56.71	127.59	151.01	327.53	304.60
$C_{6\text{vdW2D}}^{\text{BB}}$	–	18.47	20.99	6.67	97.22	140.19	5.85	7.37	11.21	23.12
$R_{0\text{vdW2D}}^{\text{A}}$	3.08	3.62	3.70	3.14	3.49	3.54	3.42	3.44	3.72	3.86
$R_{0\text{vdW2D}}^{\text{B}}$	–	3.10	3.17	2.67	3.60	3.74	2.64	2.74	2.94	3.22

the number of bands being higher than the maximum number of plane waves. In all calculations, a vacuum slab of 30 Å was used to avoid any spurious interaction between period images.

III. RESULTS AND DISCUSSION

Table I lists the derived C_6 coefficients and effective vdW radii of atoms in planar graphene-like monolayers [45,46]. An important trend is that C_6 are distinctly reduced from the free-atom values as adopted in the DFT-TS. For example, C_6 for graphene is 17.63 hartree bohr^6, ∼40% of the free-atom value, but it approaches the value of sp^2 C (25.7) estimated for an ethane molecule [40]. This contrast suggests an influence of bonding formation on the vdW interaction. Moreover, the reduction ratio of C_6 relative to that of free atom is material dependent, being 72% for h-BN, 60% for graphene and 43% for BAs. The difference between h-BN and graphene is due to their different dielectric responses, evidenced by their distinctly different optical absorption spectra [47,48]. Meanwhile, we find a reduction of effective vdW radii relative to that of free atoms, which indicates a contraction of effective atomic volume upon bonding formation. The reduction of C_6 can also be observed in buckled graphene-like monolayers. As illustrated in Table SI [33], the reduction ratio is only 4% for SnSi but can be up to 40% for GaP.

For the MoS_2, $MoSe_2$, $MoTe_2$, WS_2, WSe_2, and WTe_2 monolayers of the 2H phase, C_6 are reduced by 30–45% relative to the free-atom values (Table II). Interestingly, the metallic 1T phases of the six MX_2 have C_6 coefficients very close to that of corresponding semiconducting 2H phases (Table SII [33]), with the difference being less than 1.5%. This observation implies that the short-ranged vdW interaction in 2D materials mainly relies on the type of atom and bonding formation instead of the detailed electronic structure at the Fermi level, unlike the long-ranged vdW interaction that is sensitive to long-wavelength charge fluctuations [49]. C_6 derived for functionalized graphene-like materials, SnO and black phosphorus monolayers [50,51] are presented in Tables SIII and SIV [33]. Similarly, they are reduced with respect to the free-atom values. For instance, C_6 in black phosphorus is 91% of the free-atom value, which is a good sign in light of that the DFT-TS overestimates the interlayer energy in black phosphorus [52].

Figure 1(a) shows the interlayer vdW energy E_{vdW} per area in bilayers of graphene-like materials with an interlayer spacing of $d = 7.9$ Å. Calculations with the ACFDT-RPA establish that h-BN and AlN have the smallest E_{vdW}, while BAs, BP, and SnC have the largest. E_{vdW} for graphene (GR) ranges in the median. This variation trend cannot be understood from the free-atom's view, since C_6 of free B and Al are much higher than that of free C. As such, the DFT-TS results in the smallest E_{vdW} for graphene in Fig. 1(a), even though it has considered the effect of charge redistribution upon bonding formation. The DFT-D2 and more sophisticated

TABLE II. C_6 coefficients (in unit of hartree bohr^6) and effective vdW radii (in unit of bohr) of atoms in transition metal dichalcogenide monolayers of 2H phase derived from dielectric functions. The free-atom values as used in the TS method [14] are presented for comparison.

	MoS_2	$MoSe_2$	$MoTe_2$	WS_2	WSe_2	WTe_2
a (Å)	3.18	3.32	3.55	3.19	3.32	3.55
$C_{6\text{free}}^{\text{AA}}$	1028.73	1028.73	1028.73	847.93	847.93	847.93
$C_{6\text{free}}^{\text{BB}}$	134	210	396	134	210	396
$R_{0\text{free}}^{\text{A}}$	4.10	4.10	4.10	4.08	4.08	4.08
$R_{0\text{free}}^{\text{B}}$	3.86	4.04	4.22	3.86	4.04	4.22
$C_{6\text{vdW2D}}^{\text{AA}}$	560.21	604.60	665.97	504.90	545.11	593.81
$C_{6\text{vdW2D}}^{\text{BB}}$	72.97	123.42	256.36	79.79	135.00	277.32
$R_{0\text{vdW2D}}^{\text{A}}$	3.70	3.75	3.81	3.74	3.79	3.84
$R_{0\text{vdW2D}}^{\text{B}}$	3.49	3.70	3.92	3.54	3.75	3.98

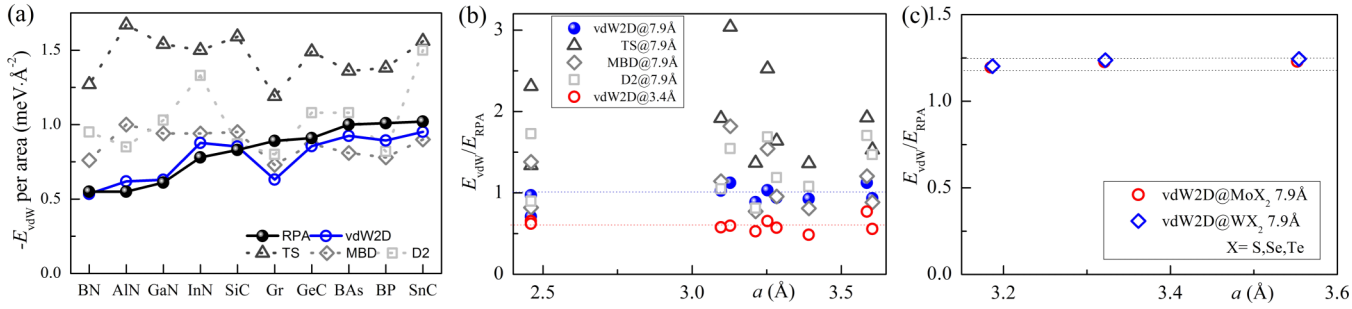

FIG. 1. (a) Interlayer vdW energies per area, E_{vdW}, in planar graphene-like bilayers of group-IV and group III-V elements at an interlayer spacing of 7.9 Å, calculated with the ACFDT-RPA, DFT-TS, DFT-MBD, DFT-D2 and DFT-vdW^{2D} methods. The abscissa labels for 2D materials are sequenced according to vdW energies calculated by the ACFDT-RPA, E_{RPA}. (b) E_{vdW}/E_{RPA} in the planar graphene-like bilayers as a function of materials lattice constant. (c) E_{vdW}/E_{RPA} in representative transition metal dichalcogenide bilayers at an interlayer spacing of 7.9 Å (distance between the two closest atomic planes in separate layers).

DFT-MBD methods cannot reproduce the variation trend from the ACFDT-RPA either, since they have not fully considered the effect of materials dielectric responses.

The DFT-vdW^{2D} provides a correct ranking of E_{vdW} among the materials. In particular, it exclusively results in a correct variation trend of E_{vdW} from *h*-BN, AlN, GaN to InN and predicts the largest E_{vdW} for BAs, BP, and SnC, both consistent with those by the ACFDT-RPA. Furthermore, the DFT-vdW^{2D} raises E_{vdW} of graphene in this rank, to a position that is higher than those of the *h*-BN, AlN, and GaN, in contrast to the other methods from which E_{vdW} of graphene is the smallest. Figure 1(b) shows the ratio of E_{vdW}/E_{RPA} as a function of materials lattice constant. With the DFT-D2, DFT-TS, and DFT-MBD methods, the calculated vdW energies show considerable deviations from those by the ACFDT-RPA, with E_{vdW}/E_{RPA} varying in the range of 0.81–1.73, 1.36–3.04, and 0.77–1.82, respectively. The unsatisfying performance of the (semi)empirical corrections is remedied by the DFT-vdW^{2D}. For the planar graphene-like materials other than graphene, the calculated E_{vdW}/E_{RPA} are concentrated into a narrow range of 0.89–1.12, whereas the deviation for graphene is slightly larger with E_{vdW}/E_{RPA} of 0.71.

A suitable interlayer spacing is crucial to a fair comparison of vdW energy. As the damping function does not affect the interlayer energy at $d = 7.9$ Å, the aforementioned ranking of E_{vdW} reflects the intrinsic vdW properties of 2D materials. On the other hand, one should not choose too large of a spacing (e.g., $d > 10$ Å), with which the vdW interactions between periodic images can induce non-negligible errors. In order to see the effect of damping, we also calculate E_{vdW}/E_{RPA} for bilayers with a near-equilibrium spacing of 3.4 Å [Fig. 1(b)]. The ratios show an overall downward shift relative to those at 7.9 Å, being distributed in the range of 0.49–0.77. The increased differences between the DFT-vdW^{2D} and ACFDT-RPA energies at 3.4 Å are mainly due to the applied damping function. For instance, f_{damp} for atomic pairs at a distance of 3.4 Å are calculated to be 0.90, 0.59, and 0.63 for graphene (C-C), SiC (Si-C), and InN (In-N), respectively. Another possible reason is the interlayer coupling at the short distance, which can influence the electronic bandgaps and dielectric functions of 2D materials. Nevertheless, the good agreement of the energetic ranking by the DFT-vdW^{2D} with that by the ACFDT-RPA is preserved at 3.4 Å.

To investigate the performance of the DFT-vdW^{2D} for 2D materials with thickness of more than one atom, we show E_{vdW}/E_{RPA} for the MoS_2, $MoSe_2$, $MoTe_2$, WS_2, WSe_2, and WTe_2 bilayers with an interlayer spacing of 7.9 Å in Fig. 1(c). Interestingly, E_{vdW}/E_{RPA} of the MX_2 bilayers are concentrated in a narrow range of 1.20–1.24. The slight overestimation of interlayer vdW energy by the DFT-vdW^{2D} is easy to understand, since the C_6 coefficient in these materials takes a mean value of $C_{6\|}$ derived from the in-plane dielectric function and the free-atom coefficient.

We then test the DFT-vdW^{2D} in evaluating the interlayer registry of graphene-like materials. As examples, Table III lists the relative binding energies per atom, E_b, of the graphene and *h*-BN bilayers in different stacking modes. The DFT-vdW^{2D} identifies a correct ground state for graphene, i.e., the AB stacking mode, in line with other methods. A greater advantage occurs for *h*-BN, of which the DFT-vdW^{2D} locate the AA′ mode near the ground line. E_b calculated with the DFT-vdW^{2D} in the AA′ mode is higher than that in the AB mode by only 0.2 meV per atom. In contrast, the energy differences between the two modes reach 1.06 and 1.12 meV per atom with the DFT-TS and DFT-D2, respectively, in conflict with the experiment that identifies the AA′ mode as the ground state of

TABLE III. Relative binding energies (in unit of meV per atom) in *h*-BN and graphene bilayers in different stacking modes, to values of the lowest-energy modes. The interlayer distances are optimized with fixed in-plane lattice constants.

	$BN_{(AB')}$	$BN_{(A'B)}$	$BN_{(AA')}$	$BN_{(AA)}$	$BN_{(AB)}$	$GR_{(AA)}$	$GR_{(AB)}$
E_{TS}	0.00	5.07	1.06	6.36	0.11	5.95	0.00
E_{D2}	2.18	10.23	1.12	11.34	0.00	6.23	0.00
E_{vdW2D}	1.06	4.63	0.20	5.21	0.00	3.85	0.00

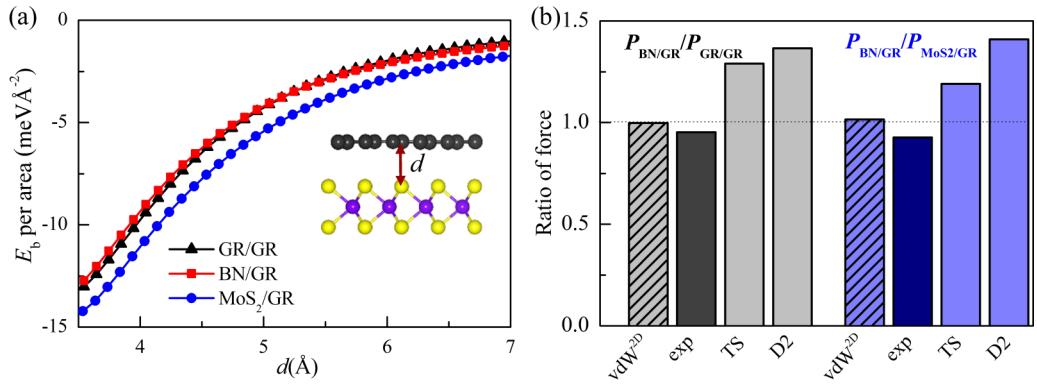

FIG. 2. (a) Binding energies per area in the GR/GR, BN/GR, and MoS_2/GR interfaces as a function of interlayer spacing, calculated with the DFT-vdW^{2D}. (b) Ratios of critical adhesion pressure at the BN/GR interface to those at the GR/GR and MoS_2/GR interfaces. The geometries for the BN/GR and GR/GR interfaces are optimized with unit cell, while that for the MoS_2/GR interface is simulated with a heterostructure consisting of 3×3 MoS_2 and 4×4 graphene with misfit strains less than 1.6%. The results by other methods and from experiments [24] are shown for comparison.

h-BN [26]. It should be noted that while the MP2 results in a ground state AA′ mode [53] with an energy lower than the AB mode by 0.12 meV per atom, the difference between the relative energies by the DFT-vdW^{2D} and MP2 is irrelevant at thermally elevated temperatures. These results suggest a need to revisit the landscape of the interlayer sliding potential for vdW crystals, potentially bringing in a remarkable influence on the interlayer superlubricity [4,54] and even fine-tuning the electronic structures [55].

The DFT-vdW^{2D} can also effectively describe the relative interfacial interactions in vdW heterostructures of 2D materials, which determines whether the contact-splitting transfer of 2D flakes from one surface to another is allowable [24]. A recent experiment has measured that the adhesion strength at the BN/GR interface is ∼0.93 times that at the MoS_2/GR interface and ∼0.95 times that at the GR/GR interface [24]. These results, however, cannot be explained by the frequently used methods, such as the DFT-D2, DFT-TS, DFT-MBD, vdW-DF, and opt88 functionals [56,57], which tend to predict larger interlayer binding energy and critical adhesion pressure at the BN/GR interface than those at another two interfaces [24]. This conflict between theory and experiment is well reconciled by the DFT-vdW^{2D}, with which the calculated binding energy at the BN/GR interface appears lower than those at the MoS_2/GR and GR/GR interfaces [Fig. 2(a)]. Furthermore, the ratio of adhesion pressures calculated from the E_b-d curves is 0.998 between BN/GR and GR/GR interfaces and 1.015 between BN/GR and MoS_2/GR interfaces [Fig. 2(b)]. Although the ratios still differ from the experimental values, they are significantly improved in comparison with those by the DFT-D2 and DFT-TS.

Another merit of the DFT-vdW^{2D} is to describe the strain dependence of interlayer vdW interaction. The C_6 coefficients for graphene and *h*-BN are found to linearly change as the applied biaxial strain changes from −4% to 4%. Specifically, a biaxial tensile strain of 4% increases C_6 of graphene and *h*-BN by 15.9% and 16.0% relative to those with −4% strain (Fig. 3). Accordingly, E_{vdW} per unit cell in the graphene and *h*-BN bilayers at a fixed distance of 3.4 Å is enhanced by 13.4% and 14.0%, respectively. To validate the revealed phenomenon, we provide the results by the *ab initio* ACFDT-RPA in Fig. 3(b). Qualitatively, the ACFDT-RPA predicts stronger interlayer vdW interactions under biaxial tensile strains, in good agreement with the DFT-vdW^{2D}. Quantitatively, the difference between the interlayer vdW energies of *h*-BN with 4% and −4% strains is 11.1 meV per cell by the ACFDT-RPA, very close to that by the DFT-vdW^{2D} (10.4 meV). For graphene, the interlayer vdW energy difference between the tensile and compressive cases by the ACFDT-RPA (19.1 meV) is higher than that by the DFT-vdW^{2D} (11.7 meV). It is worth mentioning that this strain dependence cannot be properly described by several widely used (semi)empirical methods. The DFT-D2, DFT-TS, and DFT-MBD predict an opposite and qualitatively incorrect trend, namely, the interlayer vdW interactions in the graphene and *h*-BN bilayers were weaken by biaxial tensile strains.

The variation of E_{vdW} is rooted in the change of dielectric response against strain. Taking *h*-BN as an example, the low-energy characteristic peaks of normalized imaginary dielectric function undergo a redshift and become more pronounced under applied tensile strains (Fig. S2 [33]), which result in a monotonic enhancement of dielectric functions in the whole imaginary frequency range [Fig. 3(c)]. It is surprising that C_6 of silicene exhibits a peculiar response to strain: it first decreases to a minimum and then increases as the strain changes from compression to tension [Fig. 3(a)]. This nonmonotonic change of C_6 can be understood from the interplay between the responses of in-plane and out-of-plane dielectric functions against strain. As shown in Fig. 3(d), the in-plane dielectric function of silicene increases monotonically with tensile strain. However, the out-of-plane dielectric function decreases with tensile strain, and the decrease is more pronounced in the strain range −4%–−1% but becomes milder under tensile strains.

Finally, we check the performance of the DFT-vdW^{2D} for bulk vdW crystals. Table IV lists the *c*-axis lattice constants, interlayer binding energies, and c_{33} elastic constants of representative vdW crystals, calculated with the semiempirical methods and *ab initio* ACFDT-RPA. For the *c*-axis lattice constants of graphite, *h*-BN and six MX_2, the performance of the DFT-vdW^{2D} is comparable to that of the DFT-TS. Specifically, the *c*-axis lattice constants of graphite and *h*-BN

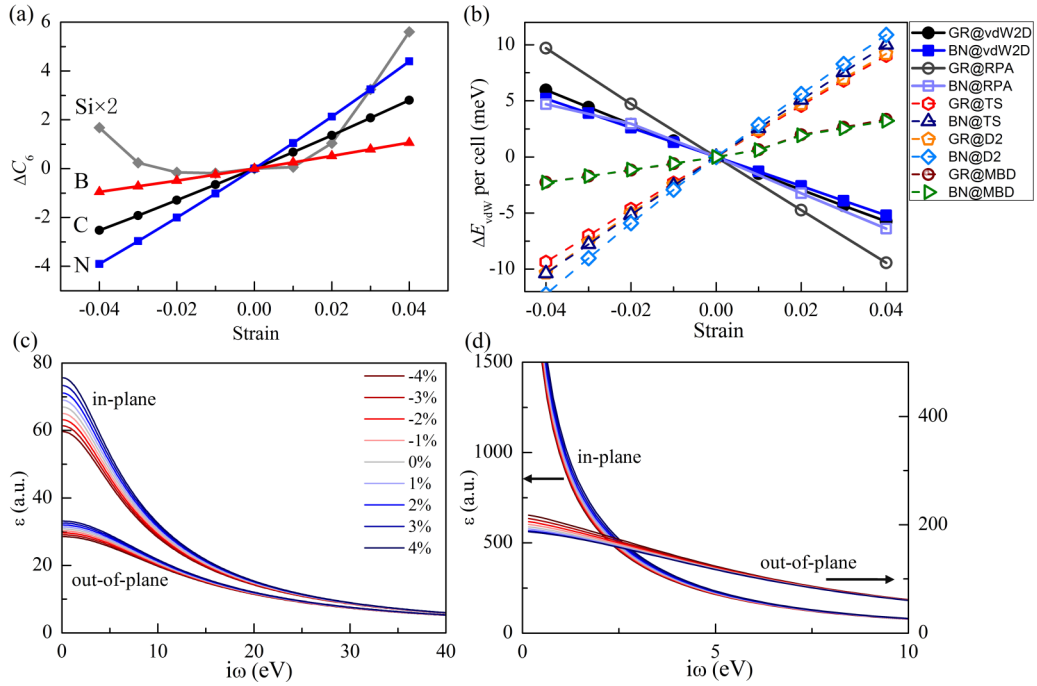

FIG. 3. (a) Dependence of C_6 coefficients of atoms (in unit of hartree bohr^6) on biaxial strain in graphene (C), *h*-BN (B and N) and silicene (Si). ΔC_6 denotes the variation of C_6 coefficient from the strain-free value. (b) Interlayer vdW energies per unit cell as a function of biaxial strain in graphene and *h*-BN bilayers, calculated with a fixed interlayer distance of 3.4 Å using the ACFDT-RPA, DFT-vdW^{2D}, DFT-TS, DFT-D2, and DFT-MBD methods. ΔE_{vdW} denotes the variation of E_{vdW} from the strain-free value. (c) Normalized in-plane and out-of-plane dielectric functions as a function of imaginary frequency of the *h*-BN monolayer under biaxial strain. (d) The same as (c) but of the silicene monolayer. For the normalization, the imaginary part of dielectric function as a function of real frequency is multiplied by the unit cell volume and then a Kramers-Kronig transformation is performed.

optimized with the DFT-vdW^{2D} deviate from the experimental values by 0.7% and 0.6%, respectively. For the six MX_2, the DFT-vdW^{2D} systematically overestimates the *c-axis* lattice constants, but the deviations from experimental results are less than 2%. The slight overestimation of *c-axis* lattice constant by the DFT-vdW^{2D} is easy to understand, as f_{damp} reduces the vdW energy at a near-equilibrium spacing. It should be noted that the MBD/FI method, a revised MBD with fractional ionic (FI) polarizabilities, shows an overall best performance for the *c-axis* lattice constants of MoS_2, $MoSe_2$, WS_2, and WSe_2 [65]. However, for the specific WS_2, the result by the DFT-vdW^{2D} is closer to the experimental value.

For the interlayer binding energies of graphite, *h*-BN, and the six MX_2, the DFT-TS suffers from large and non-negligible overestimations. Although we cannot fully remedy this deficiency, the binding energies calculated by the DFT-vdW^{2D} are more reasonable. In comparison with the benchmark ACFDT-RPA results in Ref. [18], the DFT-vdW^{2D} underestimates the binding energies of graphite and *h*-BN by 18% and 13%, respectively. In the cases of MoS_2, $MoSe_2$,

TABLE IV. *c*-axis lattice constants (in unit of Å), interlayer binding energies per unit cell E_b (in unit of meV) and c_{33} elastic constants (in unit of GPa) of bulk vdW crystals, calculated with the DFT-vdW^{2D} and DFT-TS. The listed results of experiments, ACFDT-RPA and MBD/FI calculations are taken from references. E_b is defined as the energy difference between bulk crystal and free-standing layers, instead of the interlayer binding energy as defined in the Ref. [18].

	h-BN	Graphite	MoS_2	$MoSe_2$	$MoTe_2$	WS_2	WSe_2	WTe_2
c_{exp} [58–64]	6.69	6.68	12.30	12.90	13.96	12.50	12.97	14.07
c_{vdw2D}	6.65	6.73	12.43	13.15	14.05	12.52	13.25	14.14
c_{TS}	6.67	6.70	12.04	12.77	13.99	12.20	13.02	14.05
$c_{MBD/FI}$ [65]	–	–	12.28	12.78	–	12.46	13.01	–
E_{b_RPA} [18]	−156	−192	−355.08	−368.02	–	−347.85	−372.67	–
E_{b_vdW2D}	−135.69	−156.76	−378.56	−415.57	−510.45	−371.42	−411.84	−507.24
E_{b_TS}	−345.68	−334.08	−662.64	−655.05	−702.94	−597.42	−581.74	−646.17
$E_{b\_MBD/FI}$ [65]	–	–	−358.01	−386.20	–	−314.50	−368.94	–
c_{33_vdW2D}	24.48	31.40	52.22	50.21	57.36	52.23	48.99	55.90
c_{33_TS}	37.90	67.07	56.18	45.41	32.25	46.83	34.16	36.42
c_{33_RPA} [19]	25	36	59	–	–	56	–	–

WS_2, and WSe_2, the DFT-vdW^{2D} overestimates the binding energies by less than 13%. Since the ACFDT-RPA calculations for the MX_2 were performed with fixed layer geometry [18], the reported energies should be underestimated and the accurate values could be closer to the DFT-vdW^{2D} results. The MBD/FI has also been used to calculate the binding energies of the four MX_2 and shown improved performance over the original MBD with atomic polarizabilities [65]. We note that when the MBD/FI results in smaller deviations from the ACFDT-RPA results (<9.6%), the deviations are not systematic, being either positive or negative for the four MX_2.

Regarding to the mechanical properties, the c_{33} constants of graphite and *h*-BN predicted by the DFT-vdW^{2D} are 31.40 and 24.48 GPa, respectively, being close to those given by the ACFDT-RPA (36 and 25 GPa) [19]. For the MX_2 other than MoS_2, the DFT-vdW^{2D} results in stiffer c_{33} relative to that by the DFT-TS. While the experimentally measured elastic constants may have an uncertainty, c_{33} of graphite, *h*-BN, MoS_2, and WS_2 by the DFT-vdW^{2D} seems acceptable in comparison with the experimental data summarized in Ref. [19].

IV. CONCLUSIONS

In conclusion, we have developed a DFT based semiempirical vdW method for 2D materials with the dielectric functions being incorporated via the developed Clausius-Mossotti relation. The method vastly improves the description of interlayer vdW interaction, compared to several widely used semiempirical methods. It shows notable advantages in ranking relative vdW energies of homogeneous graphene-like bilayers, rationalizing experimentally measured relative interfacial strengths of vdW heterostructures, reproducing interlayer registry of hexagonal boron nitride, and predicting a correct strain dependence of interlayer vdW energy. It also provides reasonable lattice constants, interlayer binding energies and elastic constants for typical bulk vdW crystals. The strategy holds a great potential for studying the fundamental properties and applications of 2D materials associated with ubiquitous vdW interaction.

ACKNOWLEDGMENTS

This work was supported by the National Natural Science Foundation of China (11702132, 51535005), the Natural Science Foundation of Jiangsu Province (BK20170770), the Research Fund of State Key Laboratory of Mechanics and Control of Mechanical Structures (MCMS-I-0418Y01, MCMS-0417G01), and the China Postdoctoral Science Foundation (2016M600408 and 2017T100362). X. L. is grateful to Zhuhua Zhang for valuable discussions.

[1] V. A. Parsegian, *van der Waals Forces: A Handbook for Biologists, Chemists, Engineers and Physicists* (Cambridge University Press, Cambridge, 2005).
[2] K. S. Novoselov, A. K. Geim, S. V. Morozov, D. Jiang, Y. Zhang, S. V. Dubonos, I. V. Grigorieva, and A. A. Firsov, Science **306**, 666 (2004).
[3] K. F. Mak, C. Lee, J. Hone, J. Shan, and T. F. Heinz, Phys. Rev. Lett. **105**, 136805 (2010).
[4] Z. Liu, J. Yang, F. Grey, J. Z. Liu, Y. Liu, Y. Wang, Y. Yang, Y. Cheng, and Q. Zheng, Phys. Rev. Lett. **108**, 205503 (2012).
[5] M. Yankowitz, J.-J. Wang, A. G. Birdwell, Y.-A. Chen, K. Watanabe, T. Taniguchi, P. Jacquod, P. San-Jose, P. Jarillo-Herrero, and B. J. LeRoy, Nat. Mater. **13**, 786 (2014).
[6] G. Trambly de Laissardière, D. Mayou, and L. Magaud, Nano Lett. **10**, 804 (2010).
[7] Y. Cao, V. Fatemi, S. Fang, K. Watanabe, T. Taniguchi, E. Kaxiras, and P. Jarillo-Herrero, Nature (London) **556**, 43 (2018).
[8] K. S. Kim, Y. Zhao, H. Jang, S. Y. Lee, J. M. Kim, K. S. Kim, J.-H. Ahn, P. Kim, J.-Y. Choi, and B. H. Hong, Nature (London) **457**, 706 (2009).
[9] Y. Lee, S. Bae, H. Jang, S. Jang, S.-E. Zhu, S. H. Sim, Y. I. Song, B. H. Hong, and J.-H. Ahn, Nano Lett. **10**, 490 (2010).
[10] J. Harl and G. Kresse, Phys. Rev. B **77**, 045136 (2008).
[11] X. Liu, Z. Zhang, and W. Guo, Phys. Rev. B **97**, 241411(R) (2018).
[12] C. Pisani, L. Maschio, S. Casassa, M. Halo, M. Schuetz, and D. Usvyat, J. Comput. Chem. **29**, 2113 (2008).
[13] S. Grimme, J. Comput. Chem. **27**, 1787 (2006).
[14] A. Tkatchenko and M. Scheffler, Phys. Rev. Lett. **102**, 073005 (2009).
[15] S. Cahangirov, C. Ataca, M. Topsakal, H. Sahin, and S. Ciraci, Phys. Rev. Lett. **108**, 126103 (2012).
[16] W. Gao and A. Tkatchenko, Phys. Rev. Lett. **114**, 096101 (2015).
[17] L.-F. Wang, T.-B. Ma, Y.-Z. Hu, Q. Zheng, H. Wang, and J. Luo, Nanotechnology **25**, 385701 (2014).
[18] T. Björkman, A. Gulans, A. V. Krasheninnikov, and R. M. Nieminen, Phys. Rev. Lett. **108**, 235502 (2012).
[19] T. Björkman, A. Gulans, A. V. Krasheninnikov, and R. M. Nieminen, J. Phys.: Condens. Matter **24**, 424218 (2012).
[20] J. Rafiee, X. Mi, H. Gullapalli, A. V. Thomas, F. Yavari, Y. Shi, P. M. Ajayan, and N. A. Koratkar, Nat. Mater. **11**, 217 (2012).
[21] X. Li, H. Qiu, X. Liu, J. Yin, and W. Guo, Adv. Funct. Mater. **27**, 1603181 (2016).
[22] J. N. Coleman, M. Lotya, A. O'Neill, S. D. Bergin, P. J. King, U. Khan, K. Young, A. Gaucher, S. De, R. J. Smith *et al.*, Science **331**, 568 (2011).
[23] J. N. Coleman, Acc. Chem. Res. **46**, 14 (2013).
[24] B. Li, J. Yin, X. Liu, H. Wu, J. Li, X. Li, and W. Guo, Nat. Nanotech. **14**, 567 (2019).
[25] N. Marom, J. Bernstein, J. Garel, A. Tkatchenko, E. Joselevich, L. Kronik, and O. Hod, Phys. Rev. Lett. **105**, 046801 (2010).
[26] R. S. Pease, Nature (London) **165**, 722 (1950).
[27] E. M. Lifshitz, Sov. Phys. JETP **2**, 73 (1956).
[28] D. Lu, Y. Li, D. Rocca, and G. Galli, Phys. Rev. Lett. **102**, 206411 (2009).
[29] J. R. Tessman, A. H. Kahn, and W. Shockley, Phys. Rev. **92**, 890 (1953).
[30] G.-X. Zhang, A. Tkatchenko, J. Paier, H. Appel, and M. Scheffler, Phys. Rev. Lett. **107**, 245501 (2011).
[31] L. Dell'Anna and M. Merano, Phys. Rev. A **93**, 053808 (2016).

[32] S. Cahangirov, M. Topsakal, E. Aktürk, H. Şahin, and S. Ciraci, Phys. Rev. Lett. **102**, 236804 (2009).
[33] See Supplemental Material at http://link.aps.org/supplemental/10.1103/PhysRevB.101.045428 for which includes C constants in the Clausius-Mossotti relations (Fig. S1); imaginary part of in-plane and out-of-plane normalized dielectric functions of the h-BN and silicene monolayers as a function of biaxial strain (Fig. S2); C_6 coefficients for buckled graphene-like sheets, MX_2, hydrogenated/fluorinated sheets, SnO, and black phosphorus monolayers (Tables SI–SIV).
[34] Y. Y. Hui, X. Liu, W. Jie, N. Y. Chan, J. Hao, Y.-T. Hsu, L.-J. Li, W. Guo, and S. P. Lau, ACS Nano **7**, 7126 (2013).
[35] A. J. Stone, *The Theory of Intermolecular Forces* (Oxford University Press, New York, 1996).
[36] H. B. G. Casimir and B. Polder, Phys. Rev. **73**, 360 (1948).
[37] K.T. Tang, Phys. Rev. **177**, 108 (1969).
[38] X. Chu and A. Dalgarno, J. Chem. Phys. **121**, 4083 (2004).
[39] J. P. Perdew, K. Burke, and M. Ernzerhof, Phys. Rev. Lett. **77**, 3865 (1996).
[40] S. Grimme, J. Antony, S. Ehrlich, and H. Krieg, J. Chem. Phys. **132**, 154104 (2010).
[41] A. Tkatchenko, R. A. DiStasio, Jr., R. Car, and M. Scheffler, Phys. Rev. Lett. **108**, 236402 (2012).
[42] X. Liu, J. Hermann, and A. Tkatchenko, J. Chem. Phys. **145**, 241101 (2016).
[43] G. Kresse and J. Furthmüller, Phys. Rev. B **54**, 11169 (1996).
[44] V. Blum, R. Gehrke, F. Hanke, P. Havu, V. Havu, X. Ren, K. Reuter, and M. Scheffler, Comput. Phys. Commun. **180**, 2175 (2009).
[45] H. Şahin, S. Cahangirov, M. Topsakal, E. Bekaroglu, E. Akturk, R. T. Senger, and S. Ciraci, Phys. Rev. B **80**, 155453 (2009).
[46] C.-C. Liu, W. Feng, and Y. Yao, Phys. Rev. Lett. **107**, 076802 (2011).
[47] B. Arnaud, S. Lebègue, P. Rabiller, and M. Alouani, Phys. Rev. Lett. **96**, 026402 (2006).
[48] L. Yang, Nano Lett. **11**, 3844 (2011).
[49] J. F. Dobson, A. White, and A. Rubio, Phys. Rev. Lett. **96**, 073201 (2006).
[50] S. Tsoi, P. Dev, A. L. Friedman, R. Stine, J. T. Robinson, T. L. Reinecke, and P. E. Sheehan, ACS Nano **8**, 12410 (2014).
[51] M. Xu, T. Liang, M. Shi, and H. Chen, Chem. Rev. **113**, 3766 (2013).
[52] L. Shulenburger, A. D. Baczewski, Z. Zhu, J. Guan, and D. Tománek, Nano Lett. **15**, 8170 (2015).
[53] G. Constantinescu, A. Kuc, and T. Heine, Phys. Rev. Lett. **111**, 036104 (2013).
[54] Y. Song, D. Mandelli, O. Hod, M. Urbakh, M. Ma, and Q. Zheng, Nat. Mater. **17**, 894 (2018).
[55] C.-J. Kim, L. Brown, M. W. Graham, R. Hovden, R. W. Havener, P. L. McEuen, D. A. Muller, and J. Park, Nano Lett. **13**, 5660 (2010).
[56] M. Dion, H. Rydberg, E. Schröder, D. C. Langreth, and B. I. Lundqvist, Phys. Rev. Lett. **92**, 246401 (2004).
[57] J. Klimeš, D. R. Bowler, and A. Michaelides, J. Phys.: Condens. Matter **22**, 022201 (2009).
[58] A. Brager, Acta Physicochim. URSS **7**, 669 (1937).
[59] V. Baskin and L. Meyer, Phys. Rev. **100**, 544 (1955).
[60] R. G. Dickinson and L. Pauling, J. Am. Chem. Soc. **45**, 1466 (1923).
[61] P. B. James and M. T. Lavik, Acta Cryst. **16**, 1183 (1963).
[62] D. Puotinen and R. E. Newnham, Acta Cryst. **14**, 691 (1961).
[63] R. W. G. Wyckoff, *Crystal Structures* (John Wiley and Sons, New York, 1963).
[64] B. E. Brown, Acta Cryst. **20**, 268 (1966).
[65] T. Gould, S. Lebègue, J. G. Ángyán, and T. Bučko, J. Chem. Theory Comput. **12**, 5920 (2016).